Article

Development and Application of a Poly(acrylic acid)-Grafted Styrene−Butadiene Rubber as a Binder System for Silicon-Graphite Anodes in Li-Ion Batteries

Michael J. Jolley,* Tanveerkhan S. Pathan, Alan. M. Wemyss, Ivan Prokes, Sanghamitra Moharana, Chaoying Wan, and Melanie J. Loveridge
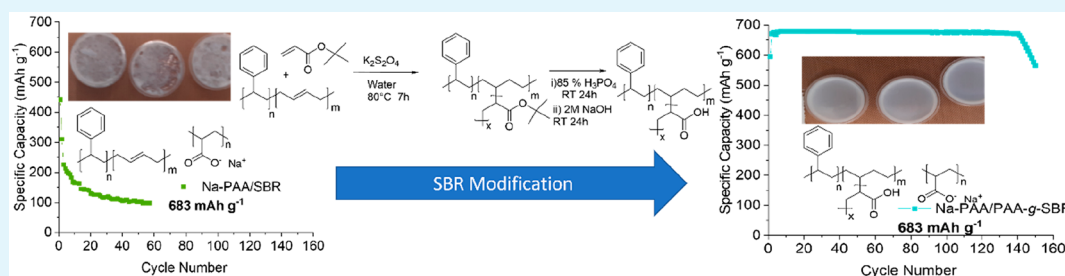
Read Online

ACCESS | Metrics & More | Article Recommendations

ABSTRACT: Silicon anodes require polymer binder systems that are both mechanically robust and electrochemically stable, to accommodate the dramatic volume expansion experienced during cycling operation. Herein, we report the use of a poly(acrylic acid)-grafted styrene−butadiene rubber (PAA-*g*-SBR) with 80% partially neutralized Na-PAA as the binder system for silicon-graphite anodes. The PAA-*g*-SBR graft copolymer was synthesized by grafting *tert*-butyl acrylate onto SBR and treating the intermediate with H_3PO_4. The PAA-*g*-SBR/Na-PAA binder system was found to provide superior electrochemical performances to that of a Na-PAA/SBR system. The Na-PAA/PAA-*g*-SBR system had a stable capacity retention of 673 mAh g^{-1} for 130 cycles, while the capacity retention of the Na-PAA/SBR system was found to decline immediately. The Na-PAA/PAA-*g*-SBR system also displayed more preferable mechanical properties, with a lower Young's modulus value and a larger strain at failure compared to that of the Na-PAA/SBR system. Overall, these findings indicate a promising and robust polymer binder system for the application of silicon anodes in the next generation of lithium-ion batteries.

KEYWORDS: lithium-ion batteries, silicon electrodes, PAA-g-SBR polymer, tert-butyl acrylate, AC impedance, electrode adhesion, energy storage application

INTRODUCTION

To meet the future energy demands of electric vehicles, the next generation of anodes in lithium-ion batteries (LIBs) should have a minimal specific capacity of 1000 mAh g^{-1}.[1] Silicon is a promising candidate for this, as it has a high specific capacity of 3579 mAh g^{-1} and is an abundant element within the earth's crust.[2] Unfortunately, the commercialization of silicon-dominant anodes has been hindered, owing to its volume expansion/contraction of up to 280 vol % when charged and discharged.[3] Over the battery's life cycle, the electrode's microstructure becomes cracked and pulverized, resulting in compromised lifetimes and accelerated capacity fades.[4]

Polymer binders are crucial materials in electrodes in order to maintain the microstructure during cycling, as they provide the necessary cohesion and adhesion strengths between the layers of active material, conductive additives, and current collector.[5] However, the traditional anode polymer binder system of poly(vinylidene fluoride) (PVdF) is ineffective for deployment in silicon anodes.[6] Primarily, this is due to PVdF only forming weak van der Waals interactions with the surface of the silicon active material and, as such, is unable to maintain the electrode's microstructure during cycling.[1] Alternatives to PVdF include poly(acrylic acid) (PAA) and carboxymethyl cellulose (CMC), which both contain carboxylic acid groups.[6] These groups form strong hydrogen-bonding and covalent interactions with the surface of the silicon active material, which provides the high adhesion strength required to
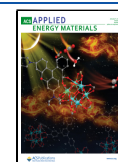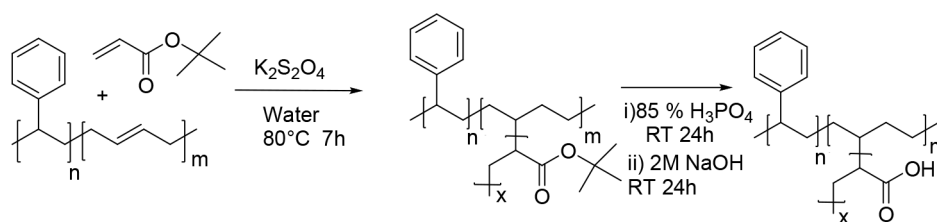
Figure 1. Propsed reaction scheme of grafting of *tert*-butyl acrylate on to the SBR seed and then hydrolyzing the *tert*-butyl acrylate group.

maintain the electrode's microstructure during cycling.[7] However, the use of PAA as the binder system requires the capacity of the anode to be limited, as PAA is mechanically brittle and cannot undertake the strain from excessive volume expansion.[8]

One strategy to overcome this is to develop a complex self-healing binder system, as proposed and demonstrated by Hu et al.[9] Another more simple strategy is to develop a binder system with a related or analogous chemistry to that of PAA, so that it can provide the necessary high adhesion strength. Additionally, a styrene butadiene rubber latex (SBR) component should also be incorporated, as this would introduce an element of flexibility to decrease the dominant rigidity of the PAA.[10] SBR is a water-based elastomer, which has been used to blend with CMC to improve the flexibility of CMC graphite anodes.[11] There have also been reports of CMC/SBR systems being used as silicon/graphite anodes, including work by Hong et al.[12] and Lee et al.[13] However, the use of PAA with SBR as the binder system is rarely reported within the literature, and in the rare cases in which it is, a third polymer is added. This includes the work by Wang et al., who used poly(vinyl alcohol) (PVA) with PAA and SBR in a ratio of 1:9:1 as the binder system for silicon anodes,[14] as well as the work by Song et al. who used partially neutralized PAA with CMC and SBR as the binder system for graphite/silicon anodes.[15]

Unfortunately, SBR and PAA are not chemically compatible and cannot be simply mixed and used simultaneously for binder applications.[16] External to the battery field, previous studies have attempted to overcome this issue by developing a grafted SBR with PAA branches, using toluene and methanol at 60 °C, or through the use of Co-60 γ radiation.[17,18] Applying these methods to the battery field is not ideal or practical, as there are strict environmental protection regulations, which have highly restricted the use of volatile organic compound solvents within industry.[11] In this study, we synthesize a PAA-*g*-SBR copolymer, which is then used as part of an integrated binder system for silicon-graphite anodes. This is achieved through seeded-core emulsion polymerization, by grafting *tert*-butyl acrylate onto SBR and hydrolyzing away the *tert*-butyl groups with 85% phosphoric acid at room temperature (Figure 1). *tert*-Butyl acrylate is a monomer that is commonly used to produce intermediate products, as the *tert*-butyl group is considered to be a more stable leaving group.[19] In addition to this, *tert*-butyl groups are easily replaced for more desirable groups, such as a carboxylic acid, through hydrolysis.[20] The resultant PAA-*g*-SBR graft copolymer is used alongside 80% partially neutralized (Na-PAA) as a possible binder system in silicon graphite anodes.

■ EXPERIMENTAL METHODS

Syntheses of PAA-*g*-SBR Graft Copolymer. 10 mL of 43 wt % SBR (Synthomer) and 1 mL of *tert*-butyl acrylate (Sigma-Aldrich containing 10−20 ppm of monomethyl ether hydroquinone as inhibitor, 98% 128.17 g mol^{-1}) was added to a flask with 15 mL of distilled water. The mixture was stirred at 100 rpm overnight, before being purged with nitrogen for an hour to remove the dissolved oxygen. 0.129 g of K$_2$S$_2$O$_8$ (Sigma-Aldrich 270.32 g mol^{-1}) initiator was dissolved in 10 g of distilled water and added to the reaction vessel. The temperature was increased to 70 °C, and the reaction was carried out for 7 h, with the mixture being stirred at 300 rpm, before being transferred to a 100 mL high-density polyethylene (HDPE) thick-walled jar (Intertreon). The *tert*-butyl groups were hydrolyzed off by adding 6.1 g of H$_3$PO$_4$ (Chem Lab 97.99 g mol^{-1}) to the reaction mixture and leaving this to stir for 24 h at room temperature. The excess acid was removed by the addition of 20 mL of 2 M NaOH, and this was left mixing for a final 24 h.

Characterization of Graft PAA-*g*-SBR Copolymer. *FTIR.* Fourier transform infrared spectroscopy (FTIR) was conducted using an FTIR Spectrometer (Vertex 70) and was run on the polymer films of the SBR starting material and the modified SBR before and after being treated with acid. The resolution setting was 4 cm^{-1} with 80 scans between the wavenumber range of 4500−500 cm^{-1}.

NMR. Samples of SBR and modified SBR were dried, cut up, and dissolved in CDCl$_3$ as a solvent with tetramethyl silane (TMS) as an internal standard. ^{1}H NMR and diffusion-ordered spectroscopy (DOSY) of the functionalized SBR were done in a Bruker 400 MHz spectrometer. All the obtained spectra were analyzed using TopspinTM.

Mechanical Testing. Na-PAA/SBR polymer blends were developed as follows, 7.14 g of 35% Na-PAA solution and 5 g of 50% SBR were added to produce a final solid ratio of 1:1. The mixture was initially dispersed with a spatula before being mixed with a Thinky ARE-250 conditioning planetary mixer (Thinky) for 5 min at 500 rpm. The resultant Na-PAA/SBR mixes were degassed for 24 h to remove any air bubbles before being casted into a precut Teflon dish (Gilbert Curry Industrial Plastics Co Ltd.). Pure SBR and Na-PAA polymer film samples were developed by pouring 6 mL of 50% SBR or Na-PAA into the precut Teflon dish. All samples were air-dried for 24 h, before being removed from the Teflon dish, weighed, and then placed back on the Teflon sheet for further air drying. This process was repeated until a constant mass was obtained for the films.

Polymer films with a thickness of 0.25−0.45 mm were cut into tensile specimens according to ASTM D638, with a gauge length of 26 mm and a width of 3.26 mm. Tensile testing was performed using a 100 kN Instron tensile tester, 1 kN load cell, wedge grips, with a video extensometer, and at an extension rate of 5 mm/min. Young's modulus was calculated using a chord modulus fitted between 0.7% and 1.5% offset strain.

Electrode Preparation. 3 g of carbon black (C-45 Timcal C-NERGY), 15 g of graphite (BTR FC-18), and 4.28 g of 35% of Na-PAA (Synthomer) were added to 20 mL of water and mixed by hand with a spatula. The slurry was placed on an overhead high-speed homodisperser (model 2.5, PRIMIX) at 620 rpm for an hour, before being placed under an ultrasonicator probe (UP400S, SciMED) at 0.5 cycles, 65% amplitude for 15 min. 9 g of 0.02−2000 μm-sized silicon powder (E-410 Elkem) was added, and the slurry was placed back on the ultrasonicator probe at 0.5 cycles, 65% amplitude for a further 3 min. The slurry was then placed back under the overhead high-speed homodisperser at 1000 rpm for a further hour of mixing. The slurry was transferred to a Filmix mixing vessel (Filmix model 40-L PRIMIX) and was subjected to 30 s at 10 ms^{-1} and then 30 s at 25 ms^{-1}. The resultant mixture was transferred to a 100 mL high HDPE

thick-walled jar. 3 g grams of 50% SBR was added, and the slurry was placed in a Thinky mixer for 5 min at 500 rpm for the final stages of mixing. The resultant slurries were allowed to degas for 30 min.

The electrode slurries were coated onto 11 μm thick copper (Oak Mitsui, electrodeposited) using a draw-down coater (RK Instruments Ltd.) at a blade gap of 90 μm. Coatings were placed on a hot plate (Nickel Electro Clifton HP1−1D) at 50 °C for 5 min to remove most of the solvent, before being stored in a vacuum oven (Binder - VD 53 Vacuum Drying oven) with integrated vacuum pump system) at 50 °C for a period of 24 h. The above mixing procedure results in an electrode formulation with a dry mass % composition of 30:50:10:10 (silicon/graphite/conductive additive/binder). Table 1 provides an overview of the electrode formulations used in this study.

Table 1. Overview of Electrode Formulations

electrode slurry	Si (%)	Graphite (%)	C-45 (%)	(Na-PAA) (%)	SBR (%)
Na-PAA	30	50	10	10	0
Na-PAA/SBR	30	50	10	5	5
Na-PAA/PAA-*g*-SBR	30	50	10	5	5

Electrochemical Characterization. CR2032 coin cell components (Hohsen Corporation) were used to assemble anode half-cells versus lithium. Electrode coatings were dried in a vacuum oven (Binder - VD 53 Vacuum Drying oven with integrated vacuum pump system) at 50 °C for a period of 24 h. Electrodes were cut out using a 15.0 mm electrode cutter (Supplier Zhengzhou CY Scientific Instrument Co, Ltd.) and weighed out on a microbalance (Sartorius). Precut 15.6 × 0.25 mm thick lithium discs (Pi-Kem Limited) were used as counter electrodes and were stored under vacuum. The separator used was a trilayer polypropylene−polyethylene−polypropylene (Celgard 2325), which was cut into 19 mm diameter discs. All cell components were dried in a vacuum oven for 24 h before being assembled into cells. Commercial RD265 electrolyte (Soulbrain), containing 1.2 M LiPF$_6$ in ethylene carbonate (EC)/ethyl methyl carbonate (EMC) 1/3 v/v + 3% wt vinyl carbonate (VC) + 15% fluoroethylene carbonate (FEC), was used for the silicon/graphite system.

Silicon-graphite anode half-cells (vs Li/Li$^+$) were tested using a Biologic BSC-805 series potentiostat cycler using a constant current (CC) method in a 25 °C temperature-controlled oven. For the formation cycle, the cells were discharged to 5 mV and then charged to 1.0 V, at a C/20 rate. Further discharge/charge cycling was carried out at a C/5 rate between these voltage limits.

Potentio Electrochemical Impedance Spectroscopy (PEIS). Potentio electrochemical impedance spectroscopy (PEIS) was carried out using a VMP3 potentiostat (Bio-Logic), for measuring the impedance change as a function of cycle number. The test was conducted with a voltage amplitude of 10 mV, measured between frequencies of 500 kHz and 50 mHz at 50% state of charge (SoC) for each cell. The first measurement was taken after the formation cycle with an additional 10 min of relaxation time and repeated with every five cycles. ZView software was used for the impedance fitting equivalent circuit, which is outlined in Figure 2.

Adhesion-Cohesion Testing. The adhesion/cohesion strength of electrode coatings was determined by a compression/tensile adhesion test using a Zwick Roell 0.5 kN Tensile Tester with an Xforce P load cell, capacity 500 N, and Z-direction tensile test adaptor. A layer of double-sided polyacrylate tape on a polypropylene substrate (Teasfix 5696, Tesa) was placed on the lower specimen carrier. A 2 kg standard manual adhesive test pressure roller was used to ensure that the tapes were firmly stuck to the specimen. An electrode coating sample that was slightly larger than the specimen carrier was placed on top of the layer of tape with the coating side facing upward (Figure 3). A scalpel blade was used to remove the excess electrode coating, which was overhung from the specimen carrier. Electrode coating samples were divided up into 625 mm^2
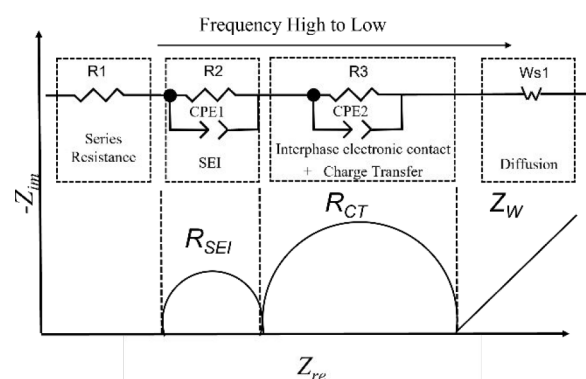

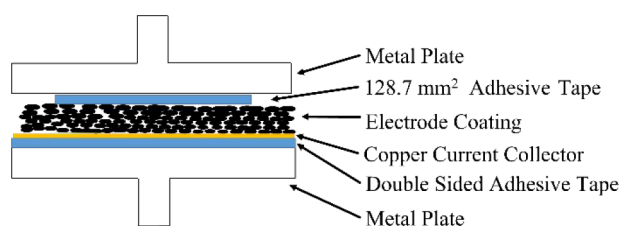**Figure 2.** Equivalent circuit model used for fitting EIS data.

Figure 3. Specimen setup for the compression/tensile adhesion test.

specimens, following the predetermined cutting guidelines on the specimen carriers.

Samples of double-sided tape (1.13 cm^2) were cut out and placed on the upper specimen plate. Samples were first compressed at 600 kPa at a velocity of 0.75 mm/min and were held for 30 s. Afterward the upper plate was pulled off at a velocity of 100 mm/min, and the maximum tensile strength was recorded at a data acquisition rate of 2 kHz.

Electrolyte Swelling Tests. Polymer film samples of the Na-PAA and SBRs were prepared by placing a coin cell polypropylene gasket casing onto a thin aluminum metal strip. The gasket was filled with 1−2 mL of polymer, and the samples were then initially air-dried for 24 h. Afterward, the samples were then placed in an oven at 60 °C overnight for further drying, after which the aluminum sheet and gasket casing were carefully removed. The samples were then dried further and weighed until a constant mass was obtained.

The polymer samples were placed in a 300 mL HDPE thick-walled jar and dried in an oven at 60 °C overnight. Samples were transferred to an argon-filled glovebox. Polymer samples were weighed using an analytical balance, before being immersed in 5 mL of commercial RD 265 electrolyte for 24 h. After 24 h the polymer/electrolyte system was filtered, and the polymer samples were removed from the electrolyte, taped, dried, and reweighed (Figure 4).

Scanning Electron Microscopy (SEM). SEM analysis was performed using a Carl Zeiss Sigma Field Emission Scanning Electron Microscope (FE-SEM) to generate the SEM images by applying an accelerated voltage of 10 kV with aperture size of 60 μm and a working distance of 7.6 mm. ASE2 detector was used for imaging. SEM images were taken of electrodes before and after cycling for the Na-PAA/SBR and Na-PAA/PAA-*g*-SBR binder systems for comparison.

■ RESULTS AND DISCUSSION

Mixing with Na-PAA. To determine if the PAA-*g*-SBR could overcome the phase-separation issue, polymer samples of Na-PAA/SBR and of Na-PAA/PAA-*g*-SBR were prepared at a weight ratio of 1:1. Phase separation was observed in the Na-PAA/SBR sample, with there being clear regions where the SBR had agglomerated in Figure 5. Meanwhile, this was found not to be the case for the Na-PAA/PAA-*g*-SBR sample, with

Figure 4. Overview of electrolyte polymer swelling tests. (a) Polymer sample initially dried and weighed, (b) polymer sample immersed in electrolyte for 24 h, (c) polymer sample removed from electrolyte, and (d) polymer samples reweighed.
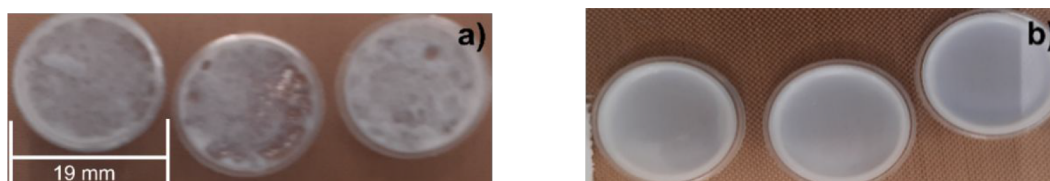

Figure 5. (a) Mixing SBR with Na-PAA resulting in phase separation. (b) Mixing SBR-*g*-PAA with Na-PAA results in no phase separation.
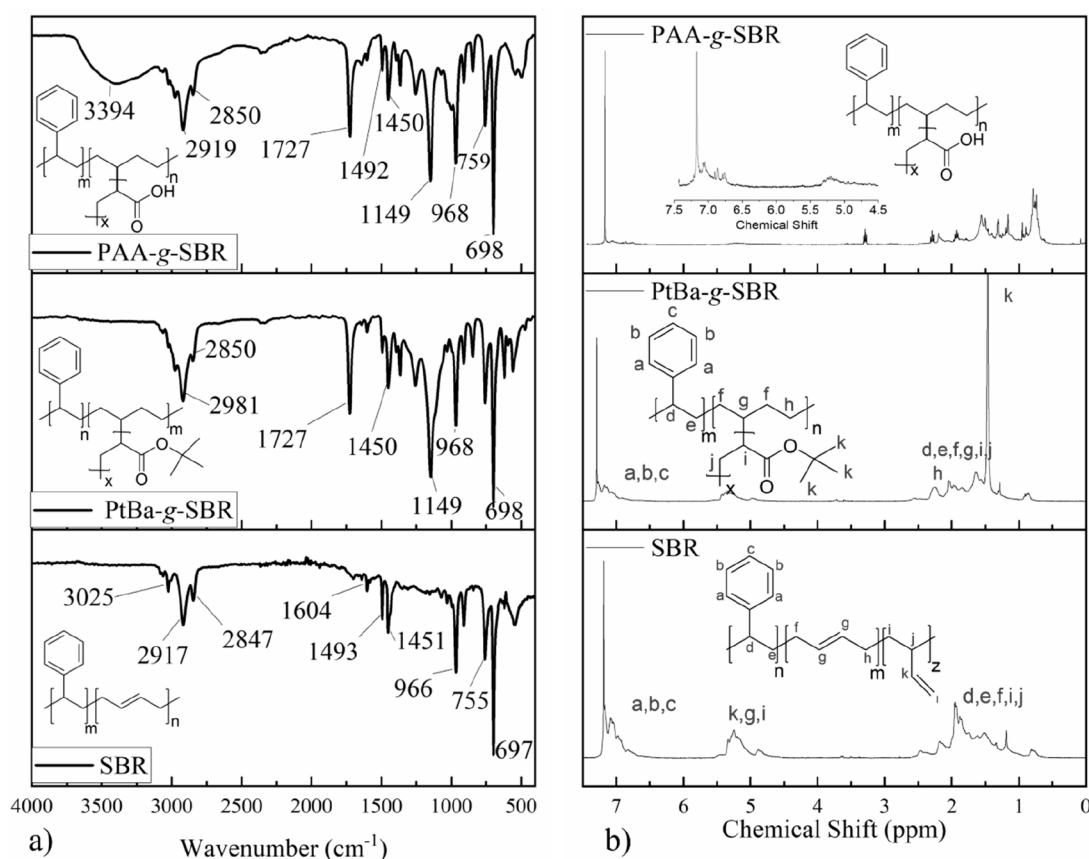

Figure 6. (a) FTIR spectra and (b) ^{1}H NMR spectra of the primary SBR starting material, PtBa-*g*-SBR intermediate, and the final PAA-g-SBR copolymer product

there being no obvious sections in which either the SBR or Na-PAA had agglomerated in Figure 5b. This suggests that the surface chemistry of the SBR had been modified, making it more chemically compatible with Na-PAA.

FTIR Charcterazation of PAA-*g*-SBR Copolymer. FTIR was performed on the primary SBR starting material, the poly(*tert*-butyl acrylate)-*g*-(styrene butadiene rubber) (Ptba-*g*-SBR) intermediate, and the final PAA-*g*-SBR copolymer product. In Figure 6a, the pure SBR sample displayed characteristic bands at 3025 cm^{-1} (aromatic C−H styrene stretching), 2917/2847 cm^{-1} (CH$_2$ aliphatic C−H stretching), 1601/1493 cm^{-1}, (C=C/C−C stretching in styrene), 1451

cm^{-1} (aromatic C=C bending in styrene units), 966 cm^{-1} (1,4-*trans*-butadiene), 755 cm^{-1} (1,4 *cis* isomers), 910 cm^{-1} (1,2-vinylbutadiene), and 697 cm^{-1} (styrene C−H bending).[21,22] The spectrum of the Ptba-*g*-SBR intermediate displayed similar characteristic bands to that of the SBR starting material, with additional peaks at 1718 cm^{-1} (C=O ester stretch) and 1150 cm^{-1} (C−O stretch) from the *tert*-butyl acrylate side chains. Finally in the PAA-*g*-SBR spectrum, a broad peak appeared at 3394 cm^{-1} (O−H stretching), indicating that the hydrolysis of the *tert*-butyl groups was successful.[20]
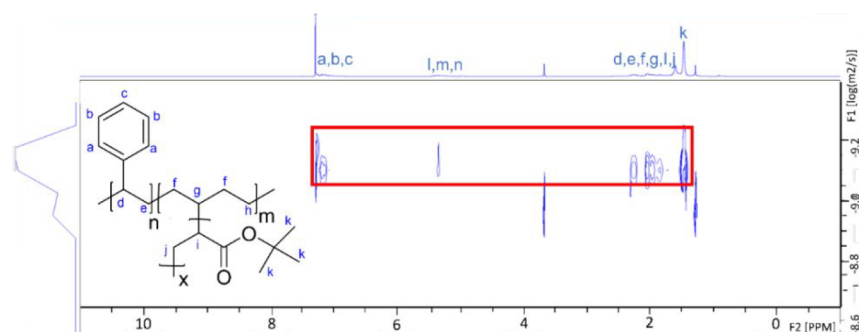
Figure 7. DOSY NMR Spectra of sample before addition of acid.

NMR Charcterazation of a PAA-*g*-SBR Copolymer. Figure 6b shows the ^{1}H NMR spectra of the SBR starting material, in which the peaks between 6.1 and 7.7 ppm belong to the aromatic hydrogens from the styrene units and from the solvent peak of the $CHCl_3$.[23] The protons associated with the alkene groups are located at 4.3–5.0 ppm ($H_2C=CHCH$ of the 1,2 unit) and 5.1–6.1 ppm ($CH_2CH=CHCH$ of the 1,4 unit and $H_2C=CHCH$ of the 1,2 unit).[24] Meanwhile, the peaks in the region of 0.5–3.0 ppm are due to the protons associated with the saturated hydrocarbons section of the backbone chain and include groups such as CH_3, CH_2, and CH.[25] The peaks in this spectrum were found to overlap, and this agrees with the NMR SBR spectra of previous studies.[26,27]

The ^{1}H NMR spectrum of PtBa-*g*-SBR was found to be very similar to that of the spectrum of the SBR starting material, with the addition of the singlet at 1.47 ppm ($C(CH_3)_3$) from the *tert*-butyl groups. However, as the ^{1}H NMR did not confirm if the *tert*-butyl group was grafted onto the SBR backbone chain or was present as part of a separate polymer, a diffusion-ordered spectroscopy NMR spectrum was also obtained. In Figure 7 the protons belonging to both the SBR backbone chain and that of the *tert*-butyl acrylate are aligned in the same region of the DOSY spectrum. This indicates that they have the same diffusion coefficients, meaning that the protons from the *tert*-butyl group and from the SBR belong to the same molecule, thus providing strong evidence that the grafting was a success.[28] Finally, the singlet at 1.47 ppm was not present in the NMR spectrum of the PAA-*g*-SBR sample, therefore confirming that the *tert*-butyl groups had successfully been hydrolyzed away.[29]

Uniaxial Tensile Testing of Polymer Films. The resultant stress/strain curves from the tensile testing of the different binder systems are provided in Figure 8. The Na-PAA/SBR system was found to have the highest Young's modulus value of 209.25 MPa, which traditionally would have been viewed as an ideal binder candidate for silicon anodes. Historically, polymers with a high Young's modulus were reported as being able to provide silicon anodes with the necessary mechanical stability to deal with the volume expansion.[7] However, more recent studies claim that it is more important for the binder systems to possess a higher degree of flexibility and a larger tensile strain.[30] These properties should allow for the binder system to more effectively accommodate the huge strain caused by silicon's large volume expansion, and ensure structural stability of the electrode's microstructure.[31]

Both the stress/strain curves of the Na-PAA/PAA-*g*-SBR and Na-PAA systems in Figure 8 demonstrate typical behaviors associated with elastomer-based polymers.[32] The Na-PAA
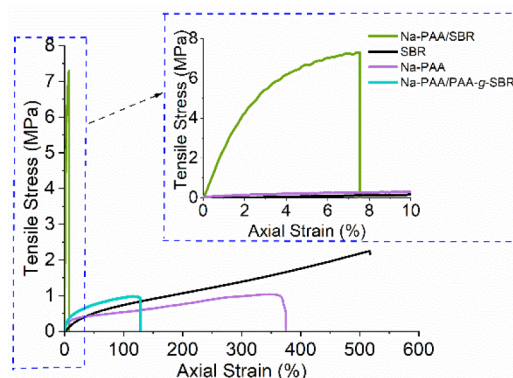

Figure 8. Stress strain curves of the different binder systems.

system had a strain at failure value of 376.99% and a Young's modulus value of 3.75 MPa (Table 2). In the case of the Na-

Table 2. Overview of Polymer Binder Systems Tensile Testing Properties[a]

binder system	Young's modulus (MPa)	strain at failure (%)	stress at failure (MPa)
Na-PAA	3.75 ± 1.74	376.99 ± 19.73	1.01 ± 0.16
Na-PAA/SBR	209.25 ± 17.36	7.55 ± 3.08	7.29 ± 0.69
Na-PAA/PAA-*g*-SBR	5.25 ± 2.91	126.51 ± 30.48	0.95 ± 0.25
SBR	0.11 ± 0.76	517.60 ± 19.63	2.15 ± 0.35

[a]The "±" refers to the standard deviation based on a minimum of four specimens.

PAA/PAA-*g*-SBR system these were 126.51% and 5.25 MPa, respectively. Regarding the Na-PAA/PAA-*g*-SBR system, this is a major improvement in stretching capability compared with the Na-PAA/SBR system, which only had a strain at failure of 7.55%. This is due to the modified SBR being more chemically compatible with Na-PAA, which allows for a more effective use of the mechanical properties from both polymer systems. Owing to these mechanical properties, the Na-PAA/PAA-*g*-SBR system should be more effective than the Na-PAA/SBR system at maintaining the electrode's microstructure. It is also important to establish that the electrode formulations contain 50% graphite, in which the graphite is designed to provide stabilization to the silicon by assisting with the accommodation of its volume expansion.[2]

Electrochemical Characterization. The voltage profiles of the first two cycles for all the binder systems are provided in Figure 9. In the first lithiation cycles, all the systems displayed
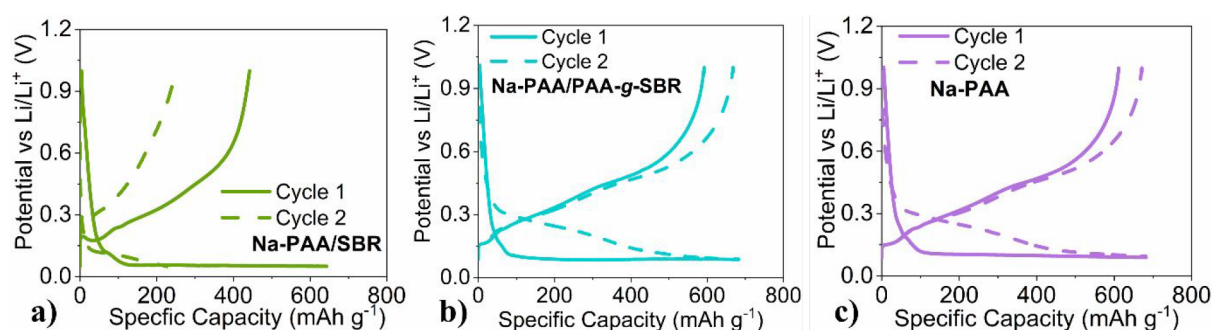
Figure 9. 1st and 2nd cycle voltage profiles of the silicon/graphite anode half cells for (a) Na-PAA/SBR, (b) Na-PAA/PAA-*g*-SBR, and (c) Na-PAA.

a decline in the voltage between 1.0 and 0.5 V and then a plateau at around 0.1 V, which is characteristic behavior of the alloying reaction between lithium and crystalline silicon.[33] For the Na-PAA and Na-PAA/PAA-*g*-SBR second cycle lithiation curves, the voltage was found to slope down from 0.3 V onward, indicating that the alloying reaction was now occurring between lithium and amorphous silicon.[34] However, in the case of the Na-PAA/SBR system, the second cycle lithiation curve does not demonstrate this same behavior, suggesting that the phase conversion from crystalline to amorphous silicon did not occur. A possible explanation for this is that the incompatibility of the two polymers caused them to phase separate out, with their agglomeration into separate regions of Na-PAA and SBR. Because of this, the binder system would have not been uniformly distributed throughout the silicon and graphite particles. This could potentially lead to the binder system not facilitating the establishment of an effective microstructure with short and long-range conductive networks. This would electrically isolate a significant proportion of the active material, and therefore, the silicon could not be lithiated sufficiently to undergo phase conversion.[35] The delithiation curves for both first and second cycles show a voltage ramp between 0.2 and 0.6 V, which is a typical response for the decomposition of the silicon lithium alloy.[33]

The longer cycling performances of the binder systems are provided in Figure 10. The initial capacity of the Na-PAA/SBR system was 442 mAh g^{-1}, before sharply declining to 310 mAh g^{-1} by cycle 2. Meanwhile, the initial capacity of the Na-PAA/PAA-*g*-SBR system was 592 mAh g^{-1}, and then by cycle 2 it
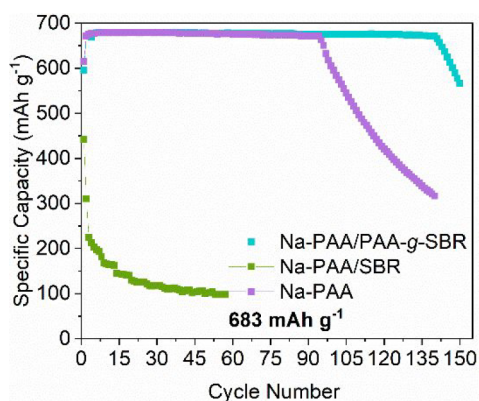
increased to 671 mAh g^{-1}. This increase in capacity from cycle 1 to cycle 2, for the Na-PAA/PAA-*g*-SBR, is due to the phase conversion to amorphous silicon, which is known to be a more favorable environment for lithium-ion diffusion kinetics.[36] By cycle 20 the capacity of the of Na-PAA/SBR system had decreased to 130 mAh g^{-1}, while after 130 cycles the capacity of the Na-PAA/PAA-*g*-SBR system was still stable at 673 mAh g^{-1}.

The only difference between the two systems is that the Na-PAA/PAA-*g*-SBR contains the modified SBR, while the Na-PAA/SBR contains the standard SBR and, as such, highlights the improvements the modified SBR makes. This is most likely to be due to the PAA-*g*-SBR system containing similar functional groups to Na-PAA. This reduces the phase separation between the two polymer systems and allows for a better overall microstructure within the electrode coating. This has improved the electrode's integrity and a microstructure that is more likely to withstand the volume expansion during cycling.

The d*Q*/d*V* versus *V* plots for cycles 1, 10, and 50 are provided in Figure 11. All of the binder systems displayed a distinctive cathodic discharge peak at 0.1 V during their first cycle, which again confirms that the alloying reaction has occurred between lithium ions and crystalline silicon.[34] In the case of the delithiation processes, the peaks occurring between 0.11 and 0.23 V derive from lithium deintercalation with the graphite ($Li_xC_6 \rightarrow C_6 + xLi^+ + xe^-$).[3,37] Meanwhile the two peaks at 0.28 and 0.47 V correspond to the phase conversion of a-$Li_{3.5}Si \rightarrow$ a-Li_2Si and a-$Li_2Si \rightarrow$ a-Si, respectively.[3] By cycles 10 and 50, significant differences were observed in the d*Q*/d*V* versus *V* plots of the different systems. In the case of the lithiation process for Na-PAA and Na-PAA/PAA-*g*-SBR systems, a shoulder peak at 0.30 V and a strong peak at 0.23 V were observed. These peaks are reported to be due to the phase conversion of a-Si $\rightarrow$ a-Li_2Si and provide a strong indication that the silicon active material has been converted from a crystalline to an amorphous state.[38] The peak present at 0.08 V is due to the conversion of a-$Li_2Si \rightarrow$ a-$Li_{3.5}Si$.[3]

Between cycles 10 and 50 in the d*Q*/d*V* versus *V* plots for the Na-PAA/SBR system, the delithiation peaks in the d*Q*/d*V* plot had essentially merged, and their peak intensity was significantly lower than that of the Na-PAA or Na-PAA/PAA-*g*-SBR system. This type of behavior in d*Q*/d*V* plots is known to be a signal of incomplete lithiation of the silicon, due to sections of the active material becoming electrically isolated.[39] This suggests that the declining cycle performance of the Na-PAA/SBR system in Figure 10 is partially due to sections of the silicon active material becoming isolated and losing
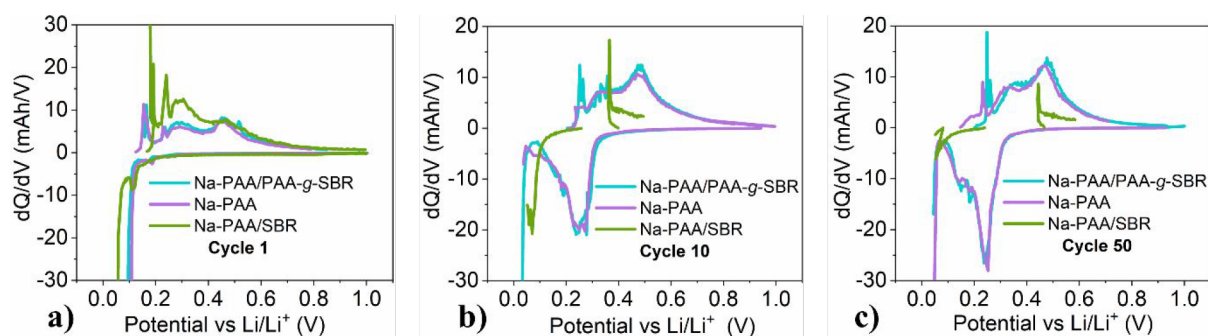

Figure 10. Longer cycling performances of silicon/graphite anode half-cells at a capacity of 683 mAh g^{-1}.

Figure 11. dQ/dV vs V plots at (a) Cycle 1, (b) Cycle 10, and (c) Cycle 50 for all the binder systems
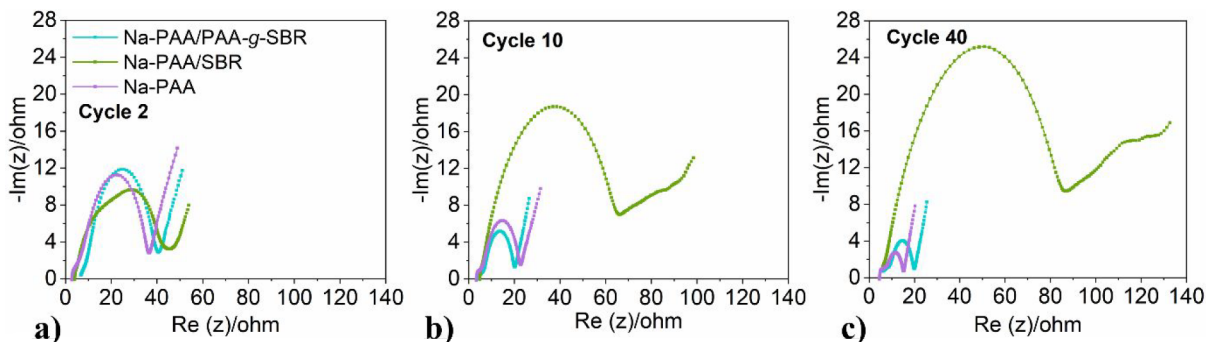

Figure 12. EIS Nyquist plots for 50% SoC at (a) cycle 2, (b) cycle 10, and (c) cycle 40 for all the binder systems.

electrical contact with the current collector. In addition to this the peaks were found to shift toward lower voltages during the lithiation process and shift toward higher voltages during the delithiation process. The shifting pattern relates to the thickening of the solid−electrolyte interface (SEI) layer, which results in increased levels of resistance within the electrodes. This observed polarization causes the charge and discharge cutoff voltages to be reached earlier, resulting in incomplete lithiation and delithiation of the active material, hence the capacity fade.[40]

Meanwhile the Na-PAA and Na-PAA/PAA-*g*-SBR systems were found to be very stable, with there being no observed significant shift in the position of the peaks. A high electrical stability within dQ/dV plots is reported to be a sign of a favorable environment for lithium ion insertion and extraction with the silicon active material.[41] The stability of these dQ/dV versus V plots at cycle 50 implies that these binder systems can effectively maintain the electrode microstructure during cycling, which is essential for providing a favorable environment for lithium-ion interaction and extraction.

Electrochemical impedance spectroscopy (EIS) was carried out to investigate the resistances within the cells of the different binder systems at 50% SoC at regular intervals. Even though the polymer binder system only contributes to a small portion of the electrode formulation, it has been well-established that it plays a vital role in determining the battery's overall performance.[32] Figure 12 provides the Nyquist plots for all the binder systems at cycles 2, 10, and 40 respectively. As explained in the methodology, the first semicircle relates to the SEI resistance (R_{SEI}), while the second larger semicircle relates to the charge transfer resistance (R_{CT}).[42] Meanwhile, the angled vertical line to the far right of the spectrum is the Warburg impedance (Zw) and is a result of lithium ions diffusing into the solid active material.[6] First, the angle of the Warburg element of the Na-PAA/SBR system is less than 45°,

which correlates to a slower lithium-ion diffusion rate, and is most likely due to the nonuniform distribution of the binder system throughout the electrode.[43] This is because SBR is reported to be quite electrically resistive and, therefore, will hinder ion diffusion if it is distributed nonuniformly and concentrated in one section of the electrode.[44] It has also been established in previous studies that a nonuniform distribution of the binder system causes sections of the active material to become inaccessible for lithium-ion intercalation, resulting in higher levels of resistances being experienced.[45]

For cycles 10 and 40 of the Na-PAA/SBR system, the angles of the Warburg elements remained below 45°. However, at lower frequencies the tails of the Warburg elements change to a significantly steeper angle. Previous studies have accredited this type of behavior to lithium ions accumulating within the graphite section of the active material of the electrode.[46] This results in an increase in resistance and decrease in capacity retention, due to a large fraction of this accumulated lithium creating a physical barrier. This then prohibits the transportation of lithium ions.[47] In cycle 40, fluctuations are observed within the Warburg elements for the Na-PAA/SBR system, indicating nonideal diffusion behavior within the electrode.[48] This has previously been reported to occur from irregular spaces throughout the active material and is most likely caused here by the poor distribution of the PAA/SBR binder system.[49]

In the case of the Na-PAA and Na-PAA/PAA-*g*-SBR systems the slopes of the Warburg elements have angles of 45°, indicating faster lithium-ion diffusion rates through these anodes.[43] For the Na-PAA and the Na-PAA/PAA-*g*-SBR systems, the R_{CT} deceased from 26.55 to 14.76 Ω and from 27.29 to 11.94 Ω, respectively. This is represented by the decrease in magnitude of the R_{CT} semicircles of these systems between cycles 2 and 10, which is due to the electrode undergoing an initial activation process, as the silicon is
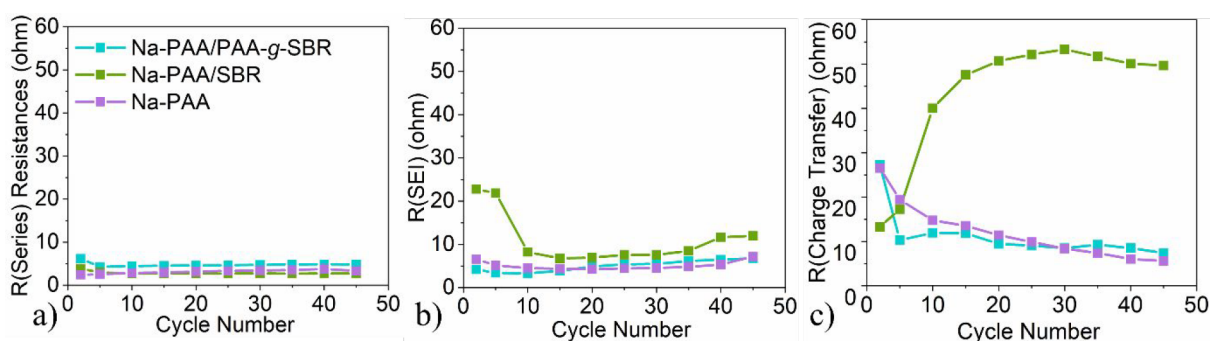
Figure 13. (a) Series resistance. (b) SEI resistance. (c) Charge transfer resistance.
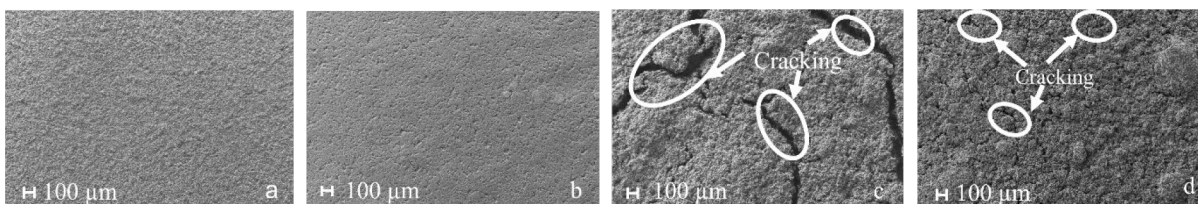

Figure 14. SEM images for (a) Na-PAA/PAA-*g*-SBR pristine, (b) Na-PAA/PAA-*g*-SBR after 150 cycles, (c) Na-PAA/SBR pristine, and (d) Na-PAA/SBR after 60 cycles.

converted from a crystalline to an amorphous state.[50] The exception to this is the Na-PAA/SBR system, in which the R_{CT} increased from 13.28 to 40.04 Ω between cycles 2 and 10, with the R_{CT} semicircles getting significantly larger. This can be explained by examining the trends in the R_s, R_{SEI}, and R_{CT} as a function of cycle number for the different binder systems, as shown in Figure 13.

The R_s values are provided in Figure 13 and, as to be expected, were relatively stable for the Na-PAA and Na-PAA/PAA-*g*-SBR systems, which indicates good ohmic contact.[51] Surprisingly, this was also found to be the case for the Na-PAA/SBR system even though it demonstrated poor capacity retentions in Figure 10. Typically, electrodes that perform poorly during cycling also experience an increase in R_s values, as a result of electrolyte degradation and particle cracking.[52] However, increases in R_s values are more commonly associated with pouch and cylindrical cells and not with coin cells as used within this study.[53] This is due to there often being an excess amount of electrolyte with coin cells and therefore demonstrating an overall slower electrolyte degradation.[54]

However, the trend in R_{SEI} values in Figure 13b indicate that the Na-PAA/SBR system produced a significantly less stable SEI layer compared to those of the Na-PAA/PAA-*g*-SBR and Na-PAA systems. First, the Na-PAA/SBR system had a significantly higher initial R_{SEI} value, and this is most likely due to the electrode having a rougher surface area for forming the SEI layer.[55] This can be observed in the pristine Na-PAA/SBR sample SEM images in Figure 14. Second, the Na-PAA/SBR system then goes on to experience a large drop in R_{SEI} between cycles 2 and 10, which previous studies have attributed to the continuous formation and decomposition of an unstable SEI layer.[56] This arises from the electrode becoming cracked and pulverized, as a consequence of silicon's large volume expansion. During this process, the SEI layer is also broken down, while a new secondary SEI layer is formed over the freshly exposed surface area of the silicon particles. This then agrees with the dramatic capacity retention decline in Figure 10, as there is a reduction in the available lithium-ion

inventory, because it is consumed for the reformation of the SEI layer. This type of behavior is another sign that the binder system is ineffective at maintaining the electrode's micro-structure during cycling.[3] It also occurs for this system, because the phase separation between Na-PAA and SBR results in a nonhomogeneous distribution of silicon, graphite, and binder throughout the electrode. As such, the graphite is unable to effectively assist with the buffering of the volume expansion of the silicon. Third, between cycles 10 and 45, the Na-PAA/SBR system experienced high R_{SEI} values compared to the Na-PAA and PAA-*g*-SBR systems, indicating that a thicker SEI layer was present for the Na-PAA/SBR system. This also agrees with the cycling performances in Figure 10, as electrodes that experience faster capacity declines are also known to experience higher R_{SEI} values.[57] Meanwhile, for the Na-PAA/PAA-*g*-SBR and Na-PAA systems, the R_{SEI} values were found to only slightly increase between cycles 2 and 45, suggesting that a stable SEI layer had been formed for these systems.[58]

Between cycles 2 and 10 the R_{CT} of the Na-PAA/SBR system rapidly increased between cycles 5 and 10 and then only gradually increased between cycles 20 and 40. The huge increase in R_{CT} is most likely due to the Na-PAA/SBR electrode becoming pulverized, which then hinders the lithium ion diffusion throughout the anode, increasing the electrode's tortuosity.[6] After cycle 20, the R_{CT} of the Na-PAA/SBR system only gradually increased between cycles 20 and 30, and then it slightly decreased from cycle 35 to 45. This can be further explained by taking into consideration the two main steps that occur during the charge transfer process. In the first step, the solvated lithium ions within the electrolyte are desolvated, and then in the second step these desolvated lithium ions are transported to the surface of the active material to accept an electron from the electrode.[59] The gradual increase in R_{CT} between cycles 20 and 30 is due to the silicon volume expansion causing the electrode to become cracked, experiencing more formation of the SEI layer, resulting in the consumption of more lithium ions. Because of this, it means that there are fewer lithium ions available to reach the surface
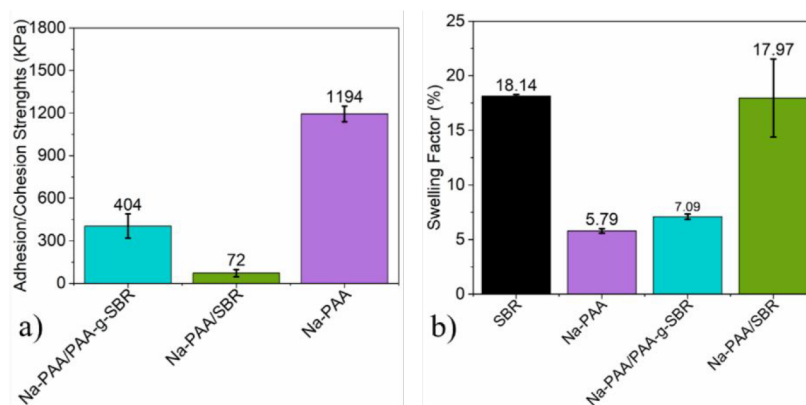
Figure 15. (a) Adhesion strengths of the electrode coatings and (b) polymer swelling tests after a 24 h immersion in electrolyte for 24 h.

of the active material and accept an electron; hence, the R_{CT} increases. Meanwhile, the decrease in R_{CT} between cycles 35 and 45 is due to the cracking, resulting in more exposed surface area of active material. Hence, it is easier for the lithium ions to accept an electron from the surface of the active material.[38]

The R_{CT} values for both the Na-PAA/PAA-g-SBR and Na-PAA systems in Figure 13c were found to sharply decline. Previous studies have acknowledged that this is because a more densely packed electrode is produced during the formation cycles, as a result of the internal stresses from silicon's large volume expansion.[38] The R_{CT} also reduces for these systems, because the phase conversion of crystalline to amorphous silicon during the initial cycles produces a more kinetically favorable environment for lithium-ion insertion.[57]

Mechanical Properties. SEM images were taken of the electrodes' coatings before and after cycling, to investigate whether the surfaces of the electrodes had experienced cracking during cycling. Cracking has been established as a clear indication of a binder system lacking the sufficient mechanical properties to maintain the electrodes' cohesive integrity during cycling.[31] Cracking was present in the pristine Na-PAA/SBR sample (Figure 14c), whereas no cracking was found to be present in the pristine Na-PAA/PAA-g-SBR sample (Figure 14a). In pristine electrodes cracking can occur when there is removal of water from the electrode coating occurring too quickly during the drying stage. This then causes the electrode coating to experience large surface tensions resulting in the formation of cracks.[67]

In the postcycled Na-PAA/SBR, sample cracks were found to be present (Figure 14d), albeit their being smaller in size compared with the cracks present in the pristine sample. This is most likely to be due to the cracks constantly closing and reopening, from the lithiation and delithiation processes during cycling.[68] Meanwhile, no cracking was observed in the postcycled Na-PAA/PAA-g-SBR sample (Figure 14b), indicating that the binder system was able to maintain the electrode's microstructure during cycling, and this correlates with the most stable electrochemical performance in Figure 10.[30] This then strongly indicates the capacity decline after 140 cycles for the Na-PAA/PAA-g-SBR system is due to the lithium counter electrode, as lithium half-cells are known to be unsuitable for long-term cycling.[69] This is because lithium undergoes a plating/stripping process at the electrode/electrolyte interfaces during cycling, with lithium ions being electrochemically reduced/oxidized to Li/Li$^+$ and deposited/removed on the metal surfaces. The plating/stripping reactions results in

infinite volume changes in the lithium metal, which cause the SEI layer to become unstable and easily crack. This then causes massive consumption of lithium and electrolyte needed to repair the layer, which eventually leads to dramatic capacity fades. However, half cells were used in this paper because they offer an easy way to evaluate new battery materials, because there is a relatively unlimited supply of usable lithium. This therefore allows for loss of active material from the electrode being investigated to be easily identified.[70]

The adhesion/cohesion strengths of the electrode coatings are provided in Figure 15a and were obtained following a method initially developed by Haselrieder following eq 1.1.[60]

$$\sigma_n = \frac{|F_{t,max}|}{A} \qquad (1.1)$$

Here, σ_n is the adhesion/cohesion strength, $F_{t, max}$ is the maximum tensile force, and A is the surface area of the electrode sample. The Na-PAA/SBR system had the lowest adhesion strength of 71.8 MPa, whereas for the Na-PAA/PAA-g-SBR system it was 404.6 MPa, and in the case of the Na-PAA system it was 1194.25 MPa. It is expected that the Na-PAA system will have the highest adhesion strength, as it contains double the amount of carboxylate groups compared to the other systems. It is these carboxylate groups that provide the strong interactions with the surface of the silicon active material. The Na-PAA/SBR system had the lowest adhesion strength, which is probably caused by the Na-PAA and SBR being chemically incompatible, causing the polymers to phase separate out and producing an overall poorer quality of electrode coating. The low adhesion strength of the Na-PAA/SBR system probably contributed to its poor cycling performance, as electrodes with lower adhesion strengths are known to undergo delamination between the active material and the current collector. This then causes a loss in electrical contact between the active material and current collector, resulting in poor cycling performances.[61]

Polymer Binder Systems Electrolyte Swelling. Polymer-electrolyte swelling tests were carried out to investigate the lithium-ion transport efficiencies of the different binder systems. The swelling factors (SW) are provided in Figure 15b and were determined by eq 1.2.[62]

$$SW(\%) = \frac{M_F - M_I}{M_I} \times 100 \qquad (1.2)$$

Here, M_F is the mass of the sample following immersion in electrolyte, and M_I is the mass of the sample before being

immersed in electrolyte.[62] The pure Na-PAA system had a relatively low SW value of 5.79%, which is due to the interactions between the polymer chains being more favorable than those of the interactions between the polymer chains and the electrolyte molecules.[63] Meanwhile, the pure SBR sample had a much higher SW value of 18.14%, while the SW values for the Na-PAA/PAA-*g*-SBR and Na-PAA/SBR systems were 7.59 and 17.97%, respectively. The Na-PAA/SBR system had the highest SW value of 17.97% as well as the greatest degree in variation in the values obtained. This is probably due to the Na-PAA and SBR polymers, strongly phase separating out and resulting in a high amount of uneven distribution of the two polymers between each sample. It is often acknowledged within the literature that binder systems with a higher degree of electrolyte uptake are more desirable than binder systems with a lower degree of electrolyte uptake.[64] This is because a higher degree of electrolyte uptake is reported to improve lithium-ion transport efficiencies, resulting in electrodes with better capacities and power performances.[65] However, in this study it is the binder systems with a lower degree of electrolyte uptake (Na-PAA and Na-PAA/PAA-*g*-SBR) that performed best during cycling. This is because polymer binder systems with a higher degree of electrolyte uptake are more likely to experience fewer molecular interactions between the polymer binder and the active material.[66] This can result in electrodes with lower adhesion/cohesion strengths, which then demonstrate less stable capacity retentions as is the case with the Na-PAA/SBR system.[5]

CONCLUSION

In this study a binder system containing the chemistries of both PAA and SBR was developed for use in silicon-graphite anodes. Due to PAA and SBR being chemically incompatible, a graft PAA-*g*-SBR copolymer was synthesized, using *tert*-butyl acrylate onto SBR in an aqueous medium at 70 °C, before hydrolyzing away the *tert*-butyl groups with aqueous-based H_3PO_4 at room temperature. The resultant PAA-*g*-SBR polymer was used alongside Synthomer's Na-PAA as the binder system for silicon-graphite anode half cells. The electrochemical performances of these electrodes were compared to those using Na-PAA/SBR and of pure Na-PAA as the binder system. The Na-PAA/PAA-*g*-SBR system was found to have a significantly superior capacity retention to that of the Na-PAA/SBR system. EIS revealed that the Na-PAA/PAA-*g*-SBR had lower levels of R_{SEI} and R_{CT} in comparison to the Na-PAA/SBR system as well as more stable peaks in the dQ/dV versus V plots in the Na-PAA/PAA-*g*-SBR compared to the Na-PAA/SBR system. This indicates that the Na-PAA/PAA-*g*-SBR binder system maintains the electrodes' microstructure more effectively during cycling and provides a more favorable environment for lithium-ion insertion. With regard to recommended further work, it is strongly recommended that focus should be applied not only to optimizing the ratio of the modified SBR to Na-PAA but also on the electrode formulation. This would allow for the development of a binder system and superior anode coating that can generate a silicon-graphite electrode that possesses the best possible electrochemical performance based on physical and chemical properties.

AUTHOR INFORMATION

Corresponding Author

Michael J. Jolley − *Energy Innovation Centre, WMG, University of Warwick, CV4 7AL Coventry, United Kingdom;* ● orcid.org/0000-0001-6963-3031; Email: m.jolley@warwick.ac.uk

Authors

Tanveerkhan S. Pathan − *Energy Innovation Centre, WMG, University of Warwick, CV4 7AL Coventry, United Kingdom;* ● orcid.org/0000-0003-4192-5109

Alan. M. Wemyss − *International Institute for Nanocomposites Manufacturing, WMG, University of Warwick, CV4 7AL Coventry, United Kingdom;* ● orcid.org/0000-0002-5919-9881

Ivan Prokes − *Department of Chemistry, University of Warwick, CV4 7AL Coventry, United Kingdom*

Sanghamitra Moharana − *Energy Innovation Centre, WMG, University of Warwick, CV4 7AL Coventry, United Kingdom*

Chaoying Wan − *International Institute for Nanocomposites Manufacturing, WMG, University of Warwick, CV4 7AL Coventry, United Kingdom;* ● orcid.org/0000-0002-1079-5885

Melanie J. Loveridge − *Energy Innovation Centre, WMG, University of Warwick, CV4 7AL Coventry, United Kingdom;* ● orcid.org/0000-0003-2908-3885

Complete contact information is available at:
https://pubs.acs.org/10.1021/acsaem.2c03489

Author Contributions

M.J.J. conducted all the experimental work, led the writing of the manuscript, and prepared the displayed figures. T.S.P. contributed to provide knowledge support for impedance data fitting and result review. A.W. contributed to design, set up the polymer syntheses, and reviewed the NMR data. I.P. contributed by running the NMR samples. S.M. contributed by running the SEM samples. C.W. contributed to manuscript revision. M.J.L. was the group leader and contributed to experimental supervision, knowledge support, and manuscript revisions.

Notes

The authors declare no competing financial interest.

ACKNOWLEDGMENTS

REFERENCES

(1) Casimir, A.; Zhang, H.; Ogoke, O.; Amine, J. C.; Lu, J.; Wu, G. Silicon-based anodes for lithium-ion batteries: Effectiveness of materials synthesis and electrode preparation. *Nano Energy* **2016**, *27* (C), 359−376.

(2) Li, P.; Kim, H.; Myung, S.; Sun, Y. Diverting Exploration of Silicon Anode into Practical Way: A Review Focused on Silicon-Graphite Composite for Lithium Ion Batteries. *Energy Storage Mater.* **2021**, *35*, 550−556.

(3) Schmerling, M.; Schwenzel, J.; Busse, M. Investigation of the degradation mechanisms of silicon thin film anodes for lithium-ion batteries. *Thin Solid Films* **2018**, *655*, 77−82.

(4) Zheng, Y.; Seifert, H. J.; Shi, H.; Zhang, Y.; Kübel, C.; Pfleging, W. 3D silicon/graphite composite electrodes for high-energy lithium-ion batteries. *Electrochim. Acta* **2019**, *317*, 502−508.

(5) Miranda, A.; Li, X.; Haregewoin, A. M.; Sarang, K.; Lutkenhaus, J.; Kostecki, R.; Verduzco, R. A Comprehensive Study of Hydrolyzed Polyacrylamide as a Binder for Silicon Anodes. *ACS Appl. Mater. Interfaces* **2019**, *11* (47), 44090−44100.

(6) Chen, C.; Chen, F.; Liu, L.; Zhao, J.; Wang, F. Cross-linked hyperbranched polyethylenimine as an efficient multidimensional binder for silicon anodes in lithium-ion batteries. *Electrochim. Acta* **2019**, *326*, No. 134964.

(7) Wei, L.; Hou, Z. High performance polymer binders inspired by chemical finishing of textiles for silicon anodes in lithium ion batteries†. *J. Mater. Chem. A* **2017**, *5* (42), 22156−22162.

(8) Kwon, T.; Choi, J. W.; Coskun, A. The emerging era of supramolecular polymeric binders in silicon anodes. *Chem. Soc. Rev.* **2018**, *47* (6), 2145−2164.

(9) Hu, S.; Wang, L.; Huang, T.; Yu, A. A conductive self-healing hydrogel binder for high-performance silicon anodes in lithium-ion batteries. *J. Power Sources* **2020**, *449*, No. 227472.

(10) Kuo, T.; Chiou, C.; Li, C.; Lee, J. In situ cross-linked poly(ether urethane) elastomer as a binder for high-performance Si anodes of lithium-ion batteries. *Electrochim. Acta* **2019**, *327*, No. 135011.

(11) Chong, J.; Xun, S.; Zheng, H.; Song, X.; Liu, G.; Ridgway, P.; Wang, J. Q.; Battaglia, V. S. A comparative study of polyacrylic acid and poly(vinylidene difluoride) binders for spherical natural graphite/LiFePO4 electrodes and cells. *J. Power Sources* **2011**, *196* (18), 7707−7714.

(12) Hong, M.; Lee, S.; Choi, S.; Mun, J. Polyimide binder for a high-energy-density composite anode electrode with graphite and silicon. *J. Electroanal. Chem.* **2020**, *871*, No. 114317.

(13) Lee, K.; Lim, S.; Go, N.; Kim, J.; Mun, J.; Kim, T. Dopamine-grafted heparin as an additive to the commercialized carboxymethyl cellulose/styrenebutadiene rubber binder for practical use of SiOx/graphite composite anode. *Scientfic Reports* **2018**, *8*, 1−9.

(14) Wang, F.; Zhang, X.; Hong, R.; Lu, X.; Zhu, Y.; Zheng, Y. High-performance anode of lithium ion batteries with plasma-prepared silicon nanoparticles and a three-component binder. *Electrochim. Acta* **2021**, *390*, No. 138809.

(15) Song, J.; Feng, Z.; Wang, Y.; Zhou, X.; Zhang, X.; Wang, K.; Xie, J. Suppressed volume variation of optimized SiOx/C anodes with PAA-based binders for advanced lithium-ion pouch cells. *Solid State Ionics* **2019**, *343*, No. 115070.

(16) Mirzaee, R.; Aref-Azar, A. Modeling and optimizing toughness and rigidity of PA6/SBR: Using compatibilizer and response surface methodology. *Polym. Test.* **2020**, *83*, No. 106346.

(17) Taheri, S.; Hassani, Y.; Sadeghi, G. M. M.; Moztarzadeh, F.; Li, M. Graft copolymerization of acrylic acid on to styrene butadiene rubber (SBR) to improve morphology and mechanical properties of SBR/ polyurethane blend. *J. Appl. Polym. Sci.* **2016**, *133* (29), 1−11.

(18) Yeganeh-Ghotbi, M.; Haddadi-Asl, V. Surface Modification of SBR and NR by Hydrophilic Monomers (I): Effect of Structural Parameters and Inhibitors. *Iran. Polym. J.* **1999**, *9*, 183−189.

(19) Walters, K. B.; Hirt, D. E. Synthesis and Characterization of a Tertiary Amine Polymer Series from Surface-Grafted Poly(tert-butyl acrylate) via Diamine Reactions. *Macromolecules* **2007**, *40* (14), 4829−4838.

(20) Sütekin, S. D.; Güven, O. Preparation of poly(tert-butyl acrylate)-poly (acrylic acid) amphiphilic copolymers via radiation-induced reversible addition− fragmentation chain transfer mediated polymerization of tert-butyl acrylate. *Polym. Int.* **2020**, *69* (8), 693−701.

(21) Jovanović, S.; Samaržija-Jovanović, S.; Marković, G.; Jovanović, V.; Adamović, T.; Marinović-Cincović, M. Ternary NR/BR/SBR rubber blend nanocomposites. *J. Thermoplast. Compos. Mater.* **2018**, *31* (2), 265−287.

(22) Chudzik, J.; Bieliński, D. M.; Jędrzejczyk, M.; Bratychak, M.; Celichowski, G.; Demchuk, Y.; Astakhova, O. Influence of Modified Epoxy Resins on Peroxide Curing, Mechanical Properties and Adhesion of SBR, NBR and XNBR to Silver Wires—Part II: Application of Carboxy-Containing Peroxy Oligomer (CPO). *Materials* **2021**, *14* (5), 1285.

(23) Tancharernrat, T.; Rempel, G. L.; Prasassarakich, P. Preparation of styrene butadiene copolymer−silica nanocomposites via differential microemulsion polymerization and NR/SBR−SiO2 membranes for pervaporation of water−ethanol mixtures. *Chem. Eng. J.* **2014**, *258*, 290−300.

(24) Choi, S.; Kim, Y.; Kwon, H. Microstructural analysis and cis−trans isomerization of BR and SBR vulcanizates reinforced with silica and carbon black using NMR and IR. *RSC Adv.* **2014**, *4*, 31113−31119.

(25) Choi, S.; Kim, Y.; Kwon, H. Analytical considerations for determination of themicrostructures of sulfur-cured solution styrene−butadiene rubbers. *Polym. Int.* **2017**, *66*, 803−808.

(26) Das, S.; Chattopadhyay, S.; Dhanania, S.; Bhowmick, A. K. Reactive grafting of 3-octanoylthio-1-propyltriethoxysilane in styrene butadiene rubber: Characterization and its effect on silica reinforced tire composites. *Polymer* **2019**, *179*, No. 121693.

(27) Hwang, K.; Mun, H.; Kim, W. Effect of Reversible Addition-Fragmentation Transfer Emulsion Styrene Butadiene Rubber (RAFT ESBR) on the Properties of Carbon Black-Filled Compounds. *Polymers* **2020**, *12*, 933.

(28) Patias, G.; Wemyss, A. M.; Atkins, C. J.; Shegiwal, A.; Efstathiou, S.; Town, J. S.; Whitfield, R.; Haddleton, D. M. Controlled synthesis of methacrylate and acrylate diblock copolymers via end-capping using CCTP and FRP. *Polym. Chem.* **2019**, *10*, 6447−6455.

(29) Wang, W.; Liu, Z.; Guo, Z.; Zhang, J.; Li, C.; Qiu, S.; Lei, X.; Zhang, Q. Hydrogen Bonding-Derived Healable Polyacrylate Elastomers via On-demand Copolymerization of n-Butyl Acrylate and tert-Butyl Acrylate. *ACS Appl. Mater. Interfaces* **2020**, *12*, 50812−50822.

(30) Deng, L.; Deng, S.; Pan, S.; Wu, Z.; Hu, Y.; Li, K.; Zhou, Y.; Li, J.; Huang, L.; Sun, S. Multivalent Amide-Hydrogen-Bond Supra-molecular Binder Enhances the Cyclic Stability of Silicon-Based Anodes for LithiumIon Batteries. *ACS Appl. Mater. Interfaces* **2021**, *13*, 22567−22576.

(31) Liu, H.; Chen, T.; Xu, Z.; Liu, Z.; Yang, J.; Chen, J. High-Safety and Long-Life Silicon-Based Lithium-Ion Batteries via a Multifunctional Binder. *ACS Appl. Mater. Interfaces* **2020**, *12*, 54842−54850.

(32) Roberts, D. R. T.; Holder, S. J. Mechanochromic systems for the detection of stress, strain and deformation in polymeric materials. *J. Mater. Chem. A* **2011**, *21* (23), 8256−8268.

(33) Kim, D. H.; Lee, H. A.; Song, Y. B.; Park, J. W.; Lee, S.; Jung, Y. S. Sheet-type Li6PS5Cl-infiltrated Si anodes fabricated by solution process for all-solid-state lithium-ion batteries. *J. Power Sources* **2019**, *426*, 143−150.

(34) Jana, M.; Ning, T.; Singh, R. N. Hierarchical nanostructured silicon-based anodes for lithium-ion battery: Processing and performance. *Mater. Sci. Eng., B* **2018**, *232−235*, 61−67.

(35) Magasinski, A.; Zdyrko, B.; Kovalenko, I.; Hertzberg, B.; Burtovyy, R.; Huebner, C. F.; Fuller, T. F.; Luzinov, I.; Yushin, G. Toward Efficient Binders for Li-Ion Battery Si-Based Anodes: Polyacrylic Acid. *ACS Appl. Mater. Interfaces* **2010**, *2* (11), 3004−3010.

(36) Ulvestad, A.; Reksten, A. H.; Andersen, H. F.; Carvalho, P. A.; Jensen, I. J. T.; Nagell, M. U.; Mæhlen, J. P.; Kirkengen, M.; Koposov, A. Y. Crystallinity of Silicon Nanoparticles: Direct Influence on the Electrochemical Performance of Lithium Ion Battery Anodes. *ChemElectroChem.* **2020**, *7* (21), 4349−4353.

(37) Guo, J.; Omar, A.; Urbanski, A.; Oswald, S.; Uhlmann, P.; Giebeler, L. Electrochemical Behavior of Microparticulate Silicon Anodes in Ether-Based Electrotyes: Why Does LiNO3 Affect Negatively? *ACS Appl. Energy Matter* **2019**, *2*, 4411−4420.

(38) Malik, R.; Huang, Q.; Silvestri, L.; Liu, D.; Pellegrini, V.; Marasco, L.; Venezia, E.; Abouali, S.; Bonaccorso, F.; Lain, M. J.; Greenwood, D.; West, G.; Shearing, P. R.; Loveridge, M. J. Synthesis of layered silicon-graphene hetero-structures by wet jet milling for

high capacity anodes in Li-ion batteries. *2D Mater.* **2021**, *8* (1), No. 015012.

(39) Choi, J.-H.; Kim, H.-K.; Jin, E.-M.; Seo, M. W.; Cho, J. S.; Kumar, R. V.; Jeong, S. M. Facile and scalable synthesis of silicon nanowires from waste rice husk silica by the molten salt process. *J. Hazard. Mater.* **2020**, *399*, No. 122949.

(40) Stetson, C.; Yin, Y.; Norman, A.; Harvey, S. P.; Schnabel, M.; Ban, C.; Jiang, C.; DeCaluwe, S. C.; Al-Jassim, M. Evolution of solid electrolyte interphase and active material in the silicon wafer model system. *J. Power Sources* **2021**, *482* (C), No. 228946.

(41) Yang, X.; Zhang, P.; Wen, Z.; Zhang, L. High performance silicon/carbon composite prepared by in situ carbon-thermal reduction for lithium ion batteries. *J. Alloys Compd.* **2010**, *496*, 403−406.

(42) Sun, Y.; Li, Y.; Yu, M.; Zhou, Z.; Zhang, Q.; Duan, B.; Shang, Y.; Zhang, C. Variable fractional order - A comprehensive evaluation indicator of lithium-ion batteries. *J. Power Sources* **2020**, *448*, No. 227411.

(43) Liu, H.; Wu, Q.; Guan, X.; Liu, M.; Wang, F.; Li, R.; Xu, J. Ionically Conductive Self-Healing Polymer Binders with Poly-(etherthioureas) Segments for High-Performance Silicon Anodes in Lithium-Ion Batteries. *ACS Appl. Energy Mater.* **2022**, *5* (4), 4934−4944.

(44) Bresser, D.; Buchholz, D.; Moretti, A.; Varzi, A.; Passerini, S. Alternative binders for sustainable electrochemical energy storage — the transition to aqueous electrode processing and bio-derived polymers. *Energy Environ. Sci.* **2018**, *11*, 3096−3127.

(45) Westphal, B. G.; Bockholt, H.; Günther, T.; Haselrieder, W.; Kwade, A. Influence of Convective Drying Parameters on Electrode Performance and Physical Electrode Properties. *ECS Trans.* **2015**, *64* (22), 57−68.

(46) Aurbach, D. Review of selected electrode−solution interactions which determine the performance of Li and Li ion batteries. *J. Power Sources* **2000**, *89* (2), 206−218.

(47) Sanders, K. J.; Aguilera, A. R.; Keffer, J. R.; Balcom, B. J.; Halalay, I. C.; Goward, G. R. Transient lithium metal plating on graphite: Operando ^{7}Li nuclear magnetic resonance investigation of a battery cell using a novel RF probe. *Carbon* **2022**, *189*, 377−385.

(48) Laschuk, N. O.; Easton, E. B.; Zenkina, O. V. Reducing the resistance for the use of electrochemical impedance spectroscopy analysis in materials chemistry. *RSC Adv.* **2021**, *11* (45), 27925−27936.

(49) Huang, J. Diffusion impedance of electroactive materials, electrolytic solutions and porous electrodes: Warburg impedance and beyond. *Electrochim. Acta* **2018**, *281*, 170−188.

(50) Guo, R.; Zhang, S.; Ying, H.; Yang, W.; Wang, J.; Han, W.-Q. New, Effective, and Low-Cost Dual-Functional Binder for Porous Silicon Anodes in Lithium-Ion Batteries. *ACS Appl. Mater. Interfaces* **2019**, *11* (15), 14051−14058.

(51) Li, B.; Zhao, W.; Yang, Z.; Zhang, C.; Dang, F.; Liu, Y.; Jin, F.; Chen, X. A carbon-doped anatase TiO_2-Based flexible silicon anode with high-performance and stability for flexible lithium-ion battery. *J. Power Sources* **2020**, *466*, No. 228339.

(52) Choi, W.; Shin, H.; Kim, J. M.; Choi, J.; Yoon, W. Modeling and Applications of Electrochemical Impedance Spectroscopy (EIS) for Lithium-ion Batteries. *J. Electrochem. Sci. Technol.* **2020**, *11*, 1−13.

(53) Abraham, J. J.; Moossa, B.; Tariq, H. A.; Kahraman, R.; Al-Qaradawi, S.; Shakoor, R. A. Electrochemical Performance of $Na_3V_2(PO_4)_2F_3$ Electrode Material in a Symmetric Cell. *Int. J. Mol. Sci.* **2021**, *22* (21), 12045.

(54) Dai, F.; Cai, M. Best practices in lithium battery cell preparation and evaluation. *Communication Materials* **2022**, *3* (1), 1−6.

(55) Zhang, Z.; Han, X.; Li, L.; Su, P.; Huang, W.; Wang, J.; Xu, J.; Li, C.; Chen, S.; Yang, Y. Tailoring the interfaces of silicon/carbon nanotube for high rate lithium-ion battery anodes. *J. Power Sources* **2020**, *450*, No. 227593.

(56) Liu, J.; Li, C.; Dong, B.; Yan, Y.; Zerrin, T.; Ozkan, M.; Ozkan, C. S. Scalable coral-like silicon powders with three-dimensional

interconnected structures for lithium ion battery anodes. *Energy Storage* **2020**, *2*, 1−11.

(57) Yu, L.; Liu, J.; He, S.; Huang, C.; Gan, L.; Gong, Z.; Long, M. A novel high-performance 3D polymer binder for silicon anode in lithiumion batteries. *J. Phys. Chem. Solids* **2019**, *135*, No. 109113.

(58) Jiang, S.; Hu, B.; Sahore, R.; Zhang, L.; Liu, H.; Zhang, L.; Lu, W.; Zhao, B.; Zhang, Z. Surface-Functionalized Silicon Nanoparticles as Anode Material for Lithium-Ion Battery. *ACS Appl. Mater. Interfaces* **2018**, *10* (51), 44924−44931.

(59) Jow, T. R.; Delp, S. A.; Allen, J. L.; Jones, J.; Smart, M. C. Factors Limiting Li^+ Charge Transfer Kinetics in Li-Ion Batteries. *J. Electrochem. Soc.* **2018**, *165* (2), A361−A367.

(60) Haselrieder, W.; Westphal, B.; Bockholt, H.; Diener, A.; Höft, S.; Kwade, A. Measuring the coating adhesion strength of electrodes for lithium-ion batteries. *Int. J. Adhes Adhes* **2015**, *60*, 1−8.

(61) Kim, J.; Jun, B. S.; Lee, S. Improvement of capacity and cyclability of Fe/Si multilayer thin film anodes for lithium rechargeable batteries. *Electrochim. Acta* **2005**, *50* (16), 3390−3394.

(62) Arafat, M. T.; Mahmud, M. M.; Wong, S. Y.; Li, X. PVA/PAA based electrospun nanofibers with pH-responsive color change using bromothymol blue and on-demand ciprofloxacin release properties. *J. Drug Deliv Sci. Technol.* **2021**, *61*, 353−377.

(63) Nguyen, Q. D.; Oh, E.; Chung, K. Nanomechanical properties of polymer binders for Li-ion batteries probed with colloidal probe atomic force microscopy. *Polym. Test.* **2019**, *76*, 245−253.

(64) Toigo, C.; Arbizzani, C.; Pettinger, K.; Biso, M. Study on Different Water-Based Binders for $Li_4Ti_5O_{12}$ Electrodes. *Molecules* **2020**, *25* (10), 2443.

(65) Yuan, J.; Sun, C. C.; Fang, L.; Song, Y.; Yan, Y.; Qiu, Z.; Shen, Y.; Li, H.; Zhu, B. A lithiated gel polymer electrolyte with superior interfacial performance for safe and long-life lithium metal battery. *J. Energy Chem.* **2021**, *55*, 313−322.

(66) Nguyen, M. H. T.; Oh, E.-S. Improvement of the characteristics of poly(acrylonitrile−butylacrylate) water-dispersed binder for lithium-ion batteries by the addition of acrylic acid and polystyrene seed. *J. Electroanal. Chem.* **2015**, *739*, 111−114.

(67) Wang, Z.; Huang, T.; Liu, Z.; Yu, A. Dopamine-modified carboxymethyl cellulose as an improved aqueous binder for silicon anodes in lithium-ion batteries. *Electrochim. Acta* **2021**, *389*, No. 138806.

(68) Wang, Y.; Dang, D.; Li, D.; Hu, J.; Zhan, X.; Cheng, Y. Effects of polymeric binders on the cracking behavior of silicon composite electrodes during electrochemical cycling. *J. Power Sources* **2019**, *438* (c), No. 226938.

(69) Yang, H.; Li, J.; Sun, Z.; Fang, R.; Wang, D. W.; He, K.; Cheng, H. M.; Li, F. Reliable liquid electrolytes for lithium metal batteries. *Energy Storage Materials* **2020**, *30*, 113−129.

(70) Schulze, M. C.; Neale, N. R. Half-Cell Cumulative Efficiency Forecasts FullCell Capacity Retention in Lithium-Ion Batteries. *ACS Energy Lett.* **2021**, *6*, 1082−1086.